Mechanism of Low-Temperature Protonic Conductivity in Bulk, High-Density, Nanometric Titanium Oxide

Ilenia G. Tredici, Filippo Maglia, Chiara Ferrara, Piercarlo Mustarelli, and Umberto Anselmi-Tamburini*

Uncovering the mechanism of low-temperature protonic conduction in highly dense nanostructured metal oxides opens the possibility to exploit the application of simple ceramic electrolytes in proton exchange fuel cells, overcoming the drawbacks related to the use of polymeric membranes. High proton conducting, highly dense (relative density 94 vol%) TiO_2 samples are prepared by a fast pressure-assisted sintering method, which allows leaving behind an interconnected network of open nanoporosity. Solid-state ^1H NMR is used to characterize the presence of strongly associated water confined in the nanopores and hydroxyl moieties bonded to the pores walls, providing a model to explain the unusually high protonic conductivity. At the lowest temperatures ($T < 55$ °C) protons hop between confined water molecules, according to a Grotthuss mechanism. The resulting conductivity values are however much higher than those of liquid water, indicating a significant increase in the charge carriers concentration. At higher temperatures (up to 450 °C) unexpected proton conduction is still present, thanks to the persistence of hydroxyl groups, derived from water chemisorption, which still produce protons by ionization. The phenomenon is strongly dependent on grain size, and not explicable by simple geometric brick-layer models, suggesting that the enhanced ionization could rely on space charge region effects.

1. Introduction

The investigation on the physical properties of bulk nanoceramics characterized by a grain size below 50 nm received a large impetus in the past few years thanks to the introduction of new sintering approaches, such as field-assisted sintering (FAST) and spark plasma sintering (SPS).[1] Significant modification in the bulk properties have been evidenced in these nanocrystalline materials.[1] The appearance of a low-temperature protonic conductivity in several bulk nanocrystalline ionic oxides, such as yttria stabilized zirconia, gadolinium or samarium doped ceria and titania, represents a particularly interesting example of these effects.[1–18] Although these oxides present the ability to incorporate protons,[15–18] none of them is usually considered a relevant protonic conductor either in the single crystal or in the bulk nonporous microcrystalline form. The low-temperature proton conductivity in highly dense nanocrystalline samples has been observed to be particularly sensitive to the grain size of the material, disappearing for grain sizes above 50–80 nm. Although a general consensus has been reached on the phenomenological aspects, the transport mechanisms responsible for this phenomenon are still debated.[1–18] Furthermore, the roles played by the chemical nature of the oxide, by the amount of lattice defects and by the residual porosity are still poorly investigated.

In this study we focus our attention on bulk nanometric TiO_2 in the anatase form, obtained through a high-pressure field assisted sintering (HP-FAST) process. Bulk nanometric anatase was recently reported to show the highest onset temperature and the highest absolute values of low-temperature proton conduction among the simple oxides so far investigated.[7] Anatase represents a particularly interesting system because it departs from the cubic fluoritic structure and from the defectivity typical of the oxides where this phenomenon has been first investigated. On the other hand, highly porous membranes or thin films of anatase have been intensively investigated for various applications requiring fast protonic conduction,[19,20] including the use as humidity sensors and as possible electrolyte material in proton exchange membrane fuel cells (PEMFCs).[21–23]

The proton conduction in porous thin films has been interpreted on the basis of the classical proton hopping mechanism (Grotthuss mechanism[24]) within a layer of water molecules adsorbed on the walls of the pore network. On the other hand, recent results obtained using fully covering TiO_2 films suggested that protons conductivity might be observed even in dense materials.[23,25] Understanding the conduction mechanism at the base of proton conduction in dense nanostructured ceramic oxides could open the possibility to optimize the features of these materials, with the aim of exploiting the application of simple ceramic electrolytes in PEMFCs, overcoming the drawbacks related to the use of polymeric membranes. In the present work, the investigations on the conduction mechanism in bulk, highly dense, nanometric samples prepared by

Dr. I. G. Tredici, Dr. F. Maglia, Dr. C. Ferrara, Prof. P. Mustarelli, Prof. U. Anselmi-Tamburini
University of Pavia
Department of Chemistry
V. Taramelli 12, I27100 Pavia, Italy
E-mail: ilenia.tredici@unipv.it

DOI: 10.1002/adfm.201400420

HP-FAST have been based on results obtained using several different characterization techniques, including AC impedance spectroscopy, BET (Brunhauer–Emmett–Teller) gas adsorption, DSC (differential scanning calorimetry) analysis and solid-state NMR. The results allowed to characterize the presence of strongly associated water confined in the nanopores and hydroxyl moieties bonded to the pores walls, providing a model to explain the unusually high protonic conductivity. The phenomenon is strongly dependent on grain size, and not explicable by simple geometric brick-layer models, suggesting that the enhanced ionization could rely on space charge region effects.

2. Results

2.1. Conductivity Measurements

Anatase nanostructured sintered samples with different grain size and relative density were prepared using a home-made HP-FAST apparatus,[26,27] according to the experimental details provided in the Supporting Information.

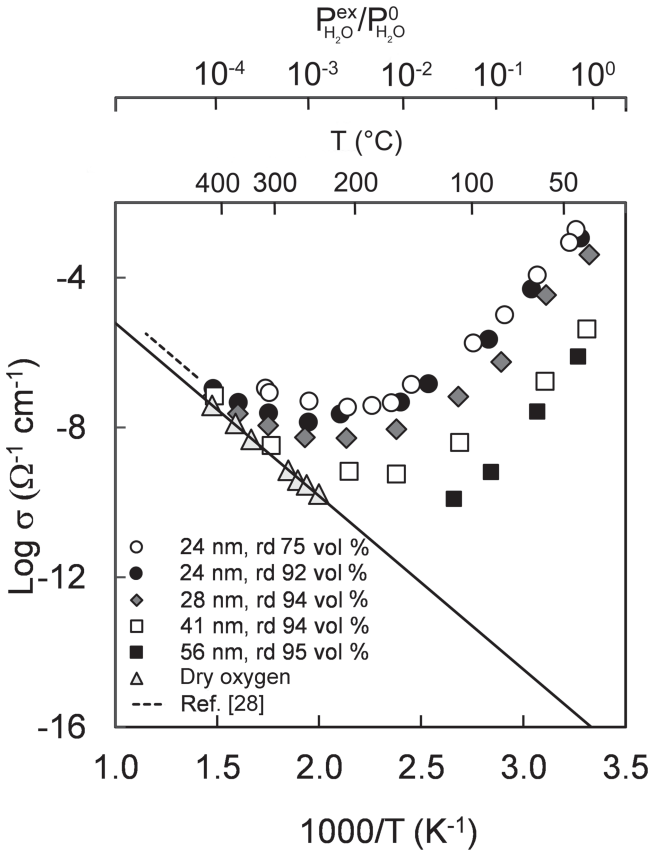

Figure 1. Influence of grain size and porosity on total conductivity, measured as a function of temperature, in dry and humidified oxygen atmosphere. The upper axis reports $P^{ex}_{H_2O}/P^{o}_{H_2O}$ in humid atmosphere as a function of temperature. $P^{o}_{H_2O}$ is the equilibrium water partial pressure at a given T; $P^{ex}_{H_2O}$ is the water partial pressure used in in our experiments ($P^{ex}_{H_2O}$ = 32 mbar).

The electrical properties of bulk nanostructured anatase samples exposed to different environments and temperatures have been discussed in a previous work[7] and will only be briefly summarized here. **Figure 1** shows the temperature dependence of the conductivity of five samples, characterized by grain size between 24 and 56 nm and relative density ranging between 75 vol% and 95 vol%, when exposed to a dry (H_2O <3 ppm) or a moist environment. The solid line indicates the conductivity of our samples under a dry oxygen atmosphere; the dashed line represents the ionic conductivity for nanometric (35 nm) anatase as reported by Knauth and Tuller in dry pure oxygen.[28] The activation energy we calculated (1.0 ± 0.1 eV) is in good agreement with theirs. It must be noted that Knauth and Tuller observed an uncommon ionic conductivity in nanometric anatase. In particular they have been able to exclude the presence of any significant electronic contribution to the conductivity in the nanometric material as long as the oxygen partial pressure is kept reasonably high. On the figure the values of relative humidity $P^{ex}_{H_2O}/P^{o}_{H_2O}$ corresponding to each temperature are also indicated. Here $P^{o}_{H_2O}$ indicates the equilibrium water pressure at each temperature, while $P^{ex}_{H_2O}$ is the water partial pressure used in in our experiments ($P^{ex}_{H_2O}$ = 32 mbar), corresponding to the equilibrium partial pressure of the water at 30 °C. Since $P^{ex}_{H_2O}$ is maintained constant throughout the experiment, the value of $P^{ex}_{H_2O}/P^{o}_{H_2O}$ decreases with increasing temperature.

Under humid atmosphere, on the other hand, a marked deviation towards higher conductivities is observed at temperatures below ≈350 °C, resulting in the inversion of the slope. As a result, the low temperature conductivity under humid atmosphere is several orders of magnitude higher than the one expected extrapolating the high temperature trend. Figure 1 also shows the strong dependence of conductivity on the grain size: for temperatures ≤ 200 °C the conductivity increases more than three orders of magnitude as the grain size is reduced from 56 to 24 nm. On the opposite, a quite limited dependence of conductivity on sample porosity has been observed: samples sintered at the same temperature (500 °C) and time (5 min), but presenting quite different relative density (92 vol% and 75 vol%) show an almost identical low temperature conductivity, despite a large difference in water uptake.[7] The protonic nature of the conduction in humid atmosphere is evidenced by the presence of a clear isotopic effect when gas saturated with D_2O is used (**Figure 2**).

Most of the characterizations described in the following are related to two samples denominated HD (high-density) and LD (low-density). Both samples have been sintered at 550 °C, and are characterized by the same grain size (28 nm), but present a relative density of 94 vol% and 75 vol%, respectively (**Figure 3**).

The kinetics of the change in resistivity produced by a switch from dry to moist gas ($P^{ex}_{H_2O}$ = 32 mbar) is shown in **Figure 4**a at four temperatures ranging between 35 and 140 °C. In this graph the points at $t = 0$ correspond to the conductivities of the samples in dry oxygen. In Figure 4b the same curves have been normalized in order to better evidence the influence of temperature that appears to be very limited. From these data the rate of conductivity change corresponding to the same degree of advancement of the process can be determined and so the activation energy. The estimated value is about 7 kJ mol^{-1}.

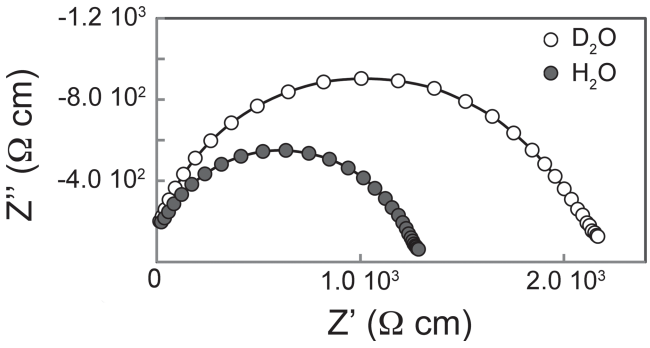

Figure 2. Impedance patterns of nanometric samples (28 nm) at 35 °C, exposed to oxygen atmosphere humidified with regular water (black circles) and deuterated water (white circles).

2.2. N_2 Adsorption Isotherms and Pore Size Distribution Analysis

The N_2 adsorption and desorption isotherms for the HD and the LD samples are reported in **Figure 5**a. A significant adsorption can be measured even for the HD sample together with a well-defined hysteresis loop. It is well known that these hysteresis loops are associated to the presence of open porosity producing capillary condensation of N_2.[29] From these data the surface area and the pore volume of the samples can be determined (see **Table 1**). The total pore volume $V_{p,tot}$ was obtained by the total amount of nitrogen adsorbed at saturation, while the surface area S_{BET} was obtained by fitting the data with a BET isotherm in the interval $0.05 < P_{N_2}/P^0_{N_2} < 0.35$. The integration method reported by Lowell[29] was applied to the desorption branch, for $0.3 < P_{N_2}/P^0_{N_2} < 1$, in order to obtain the cumulative pore volume ΣV_p and the pore distribution, as well as the

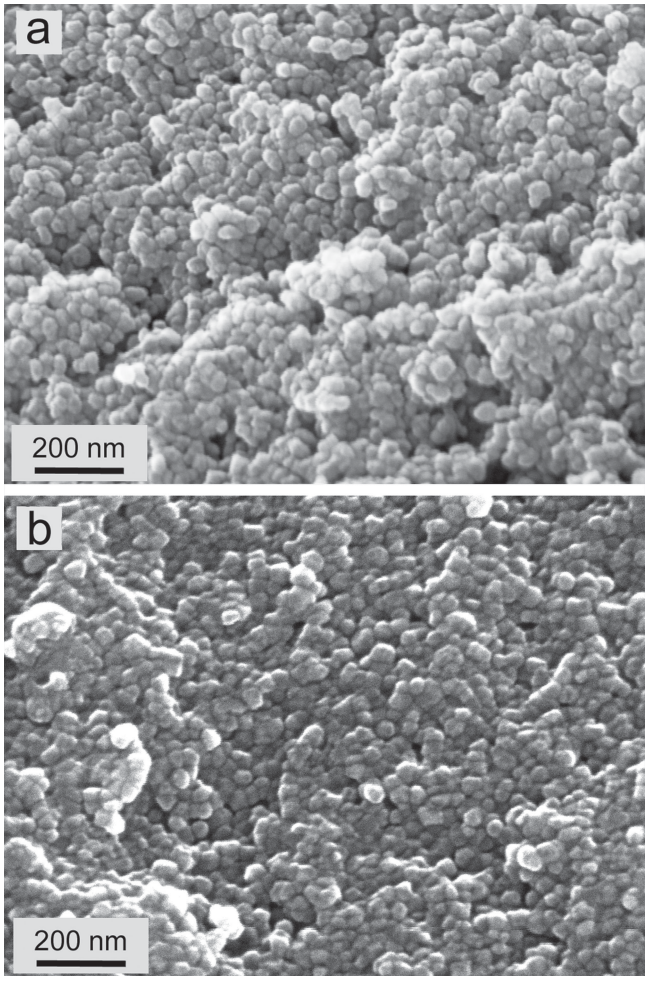

Figure 3. SEM micrographs of the a) LD and b) HD samples.

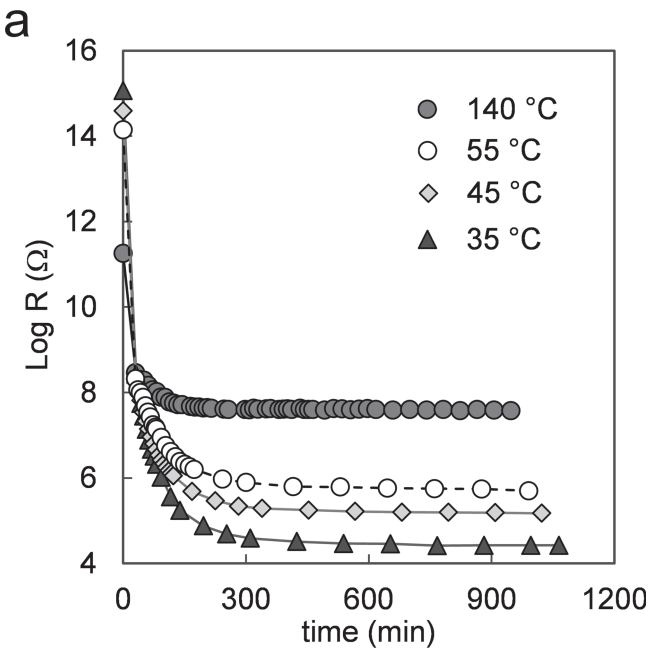

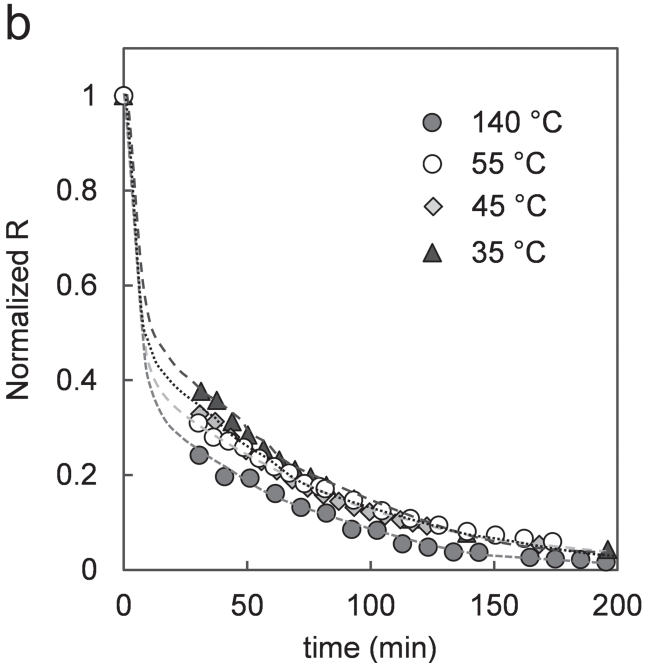

Figure 4. Kinetics of water adsorption at different temperatures, evaluated as resistance drop on the HD sample exposed to humid atmosphere: a) experimental and b) normalized data.

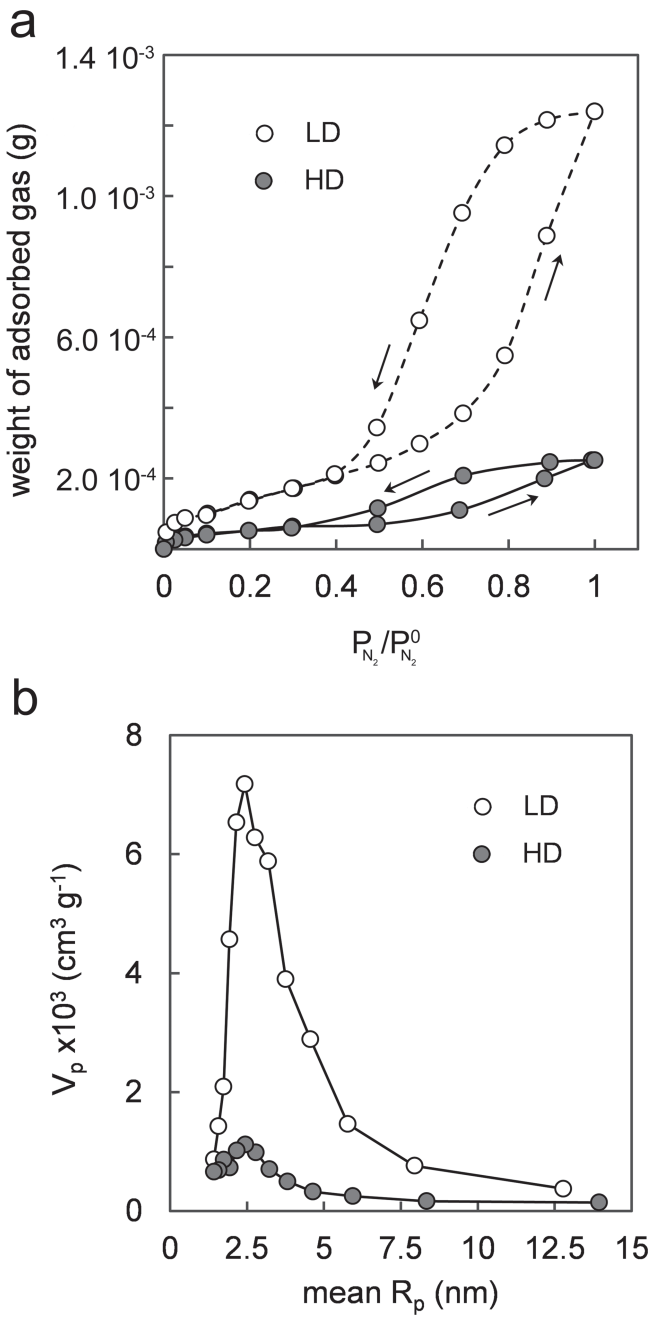

Figure 5. a) Nitrogen adsorption–desorption isotherms; b) pore distribution for LD and HD samples.

Table 1. Pore volume and surface area determined by nitrogen adsorption and desorption isotherms on HD and LD samples.

Sample	$V_{p,tot}$, [cm^3][a)]	S_{BET} [$m^2\ g^{-1}$][b)]	ΣV_p [cm^3][c)]	ΣS [$m^2\ g^{-1}$][c)]
LD	$27.8\ 10^{-3}$	8.8	$44.2\ 10^{-3}$	34.5
HD	$5.5\ 10^{-3}$	2.8	$8.1\ 10^{-3}$	7.1

[a)]from total amount of adsorbed N_2;[b)] from BET calculations;[c)] from integration method.

cumulative pore surface area ΣS.[29] Figure 5b reports the pore size distribution: its shape is similar for both samples and indicates that most of the porosity is associated to a pore radius R_p of 2–3 nm.

2.3. Melting Point of Adsorbed Water

When water is confined in narrow pores, the temperature associated to the solid-liquid transition is decreased.[30,31] A decrease of few tens of degrees has been reported in porous silica samples characterized by pores of few nanometers in size.[30,31]

DSC scans have been performed on HD and LD samples after equilibration in liquid water and subsequent freezing in liquid nitrogen. The heating rate for these experiments was 5 °C min^{-1}. For comparison, DSC scans were performed also on HD samples with larger grain size (56 nm) and on previously dried samples. The results are reported in **Figure 6**. Only one evident endothermic peak can be observed, beginning at a temperature around –12 °C for both HD and LD samples with grain size of 28 nm. The HD sample characterized by a larger grain size (56 nm) shows an endothermic peak at –3.90 °C, suggesting that bigger grains are associated to the presence of larger pores. These results confirm the presence of an open nanoporosity in our samples. In silica systems, however, a pore radius similar to the one determined on our samples with N_2 adsorption measurements (2–3 nm) would be associated to a larger reduction in the freezing point of the adsorbed water (between –20 and –30 °C). The shift that we observed (–12 °C) would be associated to a pore radius of about 5 nm. However, the agreement seems reasonable, considering than no reference data are available in the literature for titania and that N_2 adsorption based techniques have a limited sensitivity for pore radius above few nanometers.

2.4. NMR

Solid-state NMR, both static and with fast rotation (magic angle spinning, MAS) is a powerful tool for the study of the structure and dynamics of water confined in nanosized structures.[32–34] When investigating water, the most interesting nuclear probe is represented by ^1H, which produces strong signals that can be used for both chemical shift and relaxation studies. ^2H, on the other hand, can give information on the local order and dynamics, being a spin $I = 1$ nucleus with a manageable quadrupolar interaction.[35]

Figure 7a compares the ^1H NMR spectra, under static conditions, of the LD and HD samples and of the commercial TiO_2 powder (TP) after equilibration in liquid water. The peak heights have been scaled in order to show the same intensity. A quantitative estimation of the spin populations for these samples is reported in **Table 2**. In all three samples a main peak is observed in the range 5–7 ppm, with a small additional contribution 2 ppm upfield in LD and HD samples. The best-fit NMR parameters are reported in Table 2. The main peak for the commercial nanopowder (TP) is centered at 6.9 ppm and has a Lorentzian shape with FWHH = 1546 Hz, which remains practically unchanged under MAS rotation at 5 kHz. This

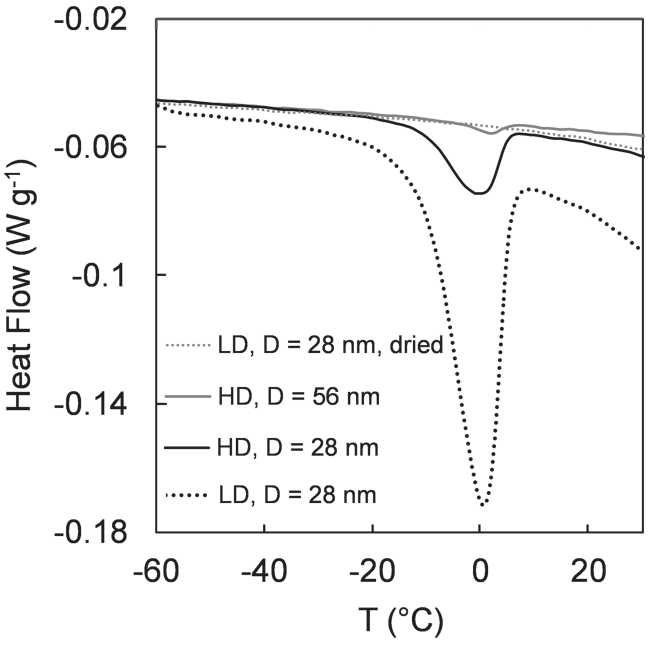

Figure 6. DSC curves showing the melting of ice confined in pores of samples with different grain size and porosity. A fourth sample was analyzed as a reference after being dried at 450 °C (LD, 28 nm, dried).

indicates that all the linewidth is due to isotropic chemical shift. Following the literature, this peak is attributed to strongly associated water (SAW), i.e. water in large clusters.[36] The main proton peaks in LD and HD samples are right-shifted (upfield) with respect to TP, falling at 6.0 and 5.7 ppm, respectively. This suggests a decrease in the size of the association/cluster of water molecules, that appears to be reduced to a dimension of about 50 nm.[37] Interestingly, the HD peak is further shifted upfield and narrower than LD, which reflects a further decrease of the confining spaces dimensions and a less disordered distribution of the hydrogen bonds. Indeed, Figure 7a clearly shows

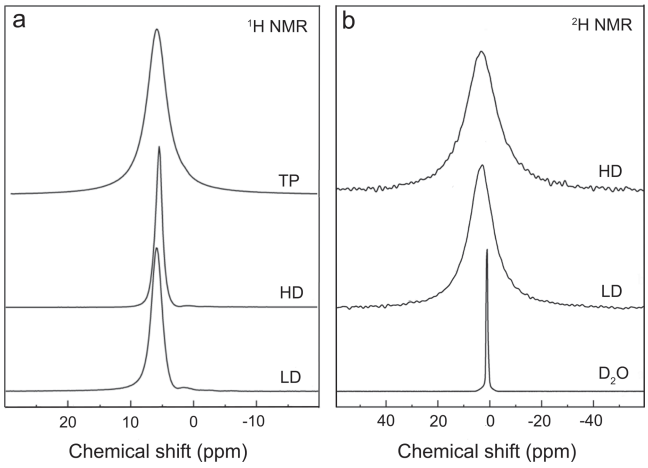

Figure 7. a) ^{1}H NMR static spectra of LD, HD and commercial TiO_2 powder (TP) after equilibration in liquid water; b) ^{2}H (^{2}H spin = 1) NMR static spectra of LD and HD samples equilibrated in D_2O, together with the spectra of pure D_2O. The fit parameters are reported in Table 2.

Table 2. NMR parameters of the spectra reported in Figure 7 and 8.

Sample	Treatment	$\delta_{(iso)}$ [ppm][a)]	FWHH [Hz][b)]	Relative intensity	Water content [mg][c)]
LD	liquid H_2O	6.01	664		
HD	liquid H_2O	5.74	434		
TP	liquid H_2O	6.93	1546		
LD	liquid D_2O	3.50	683		
HD	liquid D_2O	3.71	872		
D_2O		1.20	37		
LD (site 1)	vapour H_2O	1.81	1492	1.00	0.30 ± 0.05
LD (site 2)	vapour H_2O	6.19	1043	2.88	0.88 ± 0.05
HD (site 1)	vapour H_2O	1.81	1490	1.00	0.36 ± 0.05
HD (site 2)	vapour H_2O	6.08	1525	1.36	0.48 ± 0.05
LD (site 1)	dried 450 °C	1.81	1492	1.00	0.17 ± 0.05
LD (site 2)	dried 450 °C	5.94	3088	1.76	0.31 ± 0.05
HD (site 1)	dried 450 °C	1.82	1490	1.00	0.28 ± 0.05
HD (site 2)	dried 450 °C	5.38	3259	0.46	0.13 ± 0.05

[a)] $\delta_{(iso)}$: isotropic chemical shift; [b)] FWHH: full width at half height of the NMR line; [c)] the water content was determined as reported in the Supporting Information.

as the structure of the water present in LD and HD samples is different from that of the water adsorbed on the surface of the loose TiO_2 powder. The small peaks at ≈2 ppm are due to –OH moieties strongly bonded to the TiO_2 walls.[38] This point will be further clarified in the following.

Figure 7b shows the ^{2}H (^{2}H spin = 1) NMR static spectra of LD and HD samples equilibrated in D_2O, together with the spectra of pure D_2O. The spectra of both LD and HD samples are in the motional narrowing regime, as demonstrated by the absence of any electric quadrupolar feature. Due to the typical values for the ^{2}H quadrupolar coupling constants in the solid state (100 kHz),[39] the condition of motional narrowing implies a correlation time for local spin motion, $\tau << 10^{-7}$ s. The linewidths are about 20 times larger than that of pure D_2O due to isotropic chemical shift distribution and/or inhomogeneous susceptivity broadening not averaged by the fast ^{2}H motion. A shift downfield of about 2.5 ppm with respect to deuterated water calls for interactions with the TiO_2 walls. The fit parameters are reported in Table 2.

Figure 8 compares the ^{1}H NMR spectra under static conditions for the LD (Figure 8a) and HD (Figure 8b) samples when exposed to a humid atmosphere ($P^{ex}_{H_2O}$ = 32 mbar) at 25 °C and after dehydration in dry oxygen at 450 °C. The absolute amounts of proton moieties, expressed in milligrams, are reported in Table 2 (see Experimental Section for more details). Both samples display two peaks, which can be assigned to –OH groups strongly bonded to the TiO_2 surface (at ≈2 ppm, site 1) and to SAW (at ≈6 ppm, site 2). The assignment to bonded –OH groups is supported by the fact that the peak is retained in both HD and LD samples after the thermal treatment at 450 °C. Within the limits of the estimated errors, we can also conclude that the porous sample (LD) contains a SAW quantity (site 2) near twice than the dense one (HD), both before and after the thermal treatment at 450 °C.

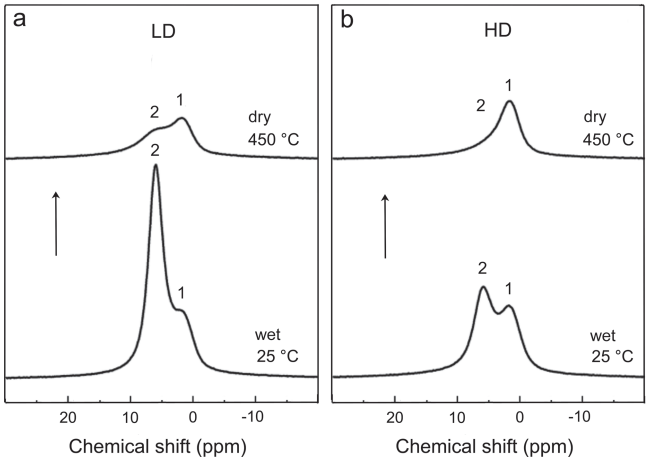

Figure 8. ^{1}H NMR spectra under static conditions for a) LD and b) HD samples when exposed to a humid atmosphere ($P^{ex}_{H_2O}$ = 32 mbar) at 25 °C (lower) and after dehydration in dry oxygen at 450 °C (upper). Site 1 (at ≈2 ppm) is attributed to –OH bonded to TiO_2 walls, site 2 (at ≈6 ppm) is attributed to SAW (strongly associated water) confined in nanopores. The absolute amounts of proton moieties, expressed in milligrams, are reported in Table 2.

3. Discussion

As recently pointed out by Shirpour et al.[16] the low-temperature protonic conductivity in nanometric oxides can in principle be interpreted considering four possible mechanisms. Protons can diffuse 1) through the crystal lattice of the material, 2) within the grain boundaries, 3) within a water layer adsorbed or condensed in the residual porosity, or 4) in the solid space charge region just underneath the surface of the pores. Earlier reports favored a transport mechanism localized at the grain boundary.[3–6,13] This conclusion was based on three main considerations: i) the solubility and low-temperature mobility of protons in the crystal lattice of simple oxides such as zirconia or ceria is too low to justify the observed conductivities,[15,17,18] ii) the phenomenon is strongly dependent on grain size, becoming particularly evident only in samples characterized by a grain size below 50 nm, and iii) it is observed also in bulk samples characterized by relative density well above 95 vol%. On the basis of these considerations, a mechanism based on the movement of protons within the grain boundary core seemed the more acceptable explanation, despite the lack of literature supporting the possibility of a large accumulation of highly mobile protons at the grain boundary in these oxides.

Our experimental results, on the other hand, strongly support another interpretation, based on the movements of protons associated to water molecules chemically or physically adsorbed on the surface of percolating nanopores. We have been able to demonstrate the presence of a significant fraction of open nanoporosity even in materials characterized by relative density of 95 vol% (HD samples). This observation is in contrast with traditional sintering models: it is in fact generally accepted that sintered materials characterized by relative density above 92–93 vol% present only close residual porosity.[40] This apparent incongruence can be possibly explained considering the peculiarities of the non-conventional fast sintering processes we used (HP-FAST). In traditional sintering (either pressureless or under pressure) the final microstructure is completely controlled by diffusion. In HP-FAST, on the opposite, the combination of low temperature and very short sintering times drastically reduces the possibility of long range diffusion, while it has been proposed that the high pressures might enhance grain sliding and grain rotation, producing a relevant plastic (and possibly superplastic) deformation.[41,42] The microstructure of ceramic materials obtained through this approach, however, is still poorly understood. Our experimental data, though, show that the HP-FAST sintering process leaves a network of open nanoporosity. This nanoporosity is accessible to water, as evidenced by the significant decrease in the melting point of the absorbed water and, above all, by the NMR results.

A further relevant argument supporting a conductivity model based on surface processes is represented by the extremely low activation energy value we observed for the process of water absorption and desorption and the associated change in conductivity (Figure 4). A value of around 7 kJ mol^{-1} is not compatible with any solid-state process, even in the grain boundaries. On the other hand, this activation energy value is very similar to the one associated to the proton mobility in liquid water,[24] supporting the idea that the low-temperature protonic conduction might be associated to a superficial conduction process confined within the layer of water molecules adsorbed or condensed in residual pores, as recently suggested by Gregori et al.[43] in the case of CeO_2 porous thin films.

3.1. Conduction Mechanism

The available models for the interpretation of the conduction within a layer of adsorbed water have been originally developed for—and applied to—ionic humidity sensors.[44,45] This application, however, involves the use of highly porous films, operating at very low temperatures in environments characterized by elevated values of $P^{ex}_{H_2O}/P^{o}_{H_2O}$. Some considerations are necessary in applying these same models to our bulk materials, characterized by a low level of porosity and a significant conductivity even in presence of low values of $P^{ex}_{H_2O}/P^{o}_{H_2O}$.

The interaction of water with ionic oxides is generally described considering chemical and physical adsorption.[46–51] Water chemical adsorption is believed to produce the formation of a monolayer of hydroxyl groups strongly bonded to the superficial Ti atoms. This layer can be completely removed only with great difficulty, requiring temperatures up to 800 °C in high vacuum.[48,50] Physical adsorption, on the other hand, results from the interaction of water molecules with the monolayer of chemically bonded hydroxyl groups and is strongly dependent on $P^{ex}_{H_2O}/P^{o}_{H_2O}$. At relatively low values of $P^{ex}_{H_2O}/P^{o}_{H_2O}$ the physically adsorbed molecules tend to form isolated clusters of superficial water molecules, that at higher values of $P^{ex}_{H_2O}/P^{o}_{H_2O}$ evolve into a multilayer film of adsorbed molecules, with characteristics very similar to bulk liquid water. Capillary condensation can also occur if nanoporosity is present, according to the Kelvin equation. It must be noted, however, that the formation of a continuous layer of physisorbed water molecules is only possible at high values of $P^{ex}_{H_2O}/P^{o}_{H_2O}$, corresponding to low temperatures in Figure 1. Literature data show

that a coverage corresponding to one monolayer can only be obtained for $P^{ex}_{H_2O}/P^{o}_{H_2O}$ values between 0.18 and 0.20,[49,50] that in Figure 1 correspond to temperatures around 55–57 °C. The capillary condensation of water in the nanopores is a process limited to even higher values of $P^{ex}_{H_2O}/P^{o}_{H_2O}$. The limiting pore diameter required for condensation of water at different temperatures, considering a $P^{ex}_{H_2O} = 32$ mbar, is reported in **Figure 9**, as calculated on the basis of the Kelvin equation. Even in the case of pores as small as 0.5 nm in radius the capillary condensation is expected to become evident only at temperatures below 50 °C. Since our BET measurements show a pore size distribution peaked around 2.5 nm in radius, it appears evident as the capillary condensation can only play a role at temperatures very close to room temperature. As recently noted by Shirpour et al.[16] the presence of complex wedge-shaped porosity (very likely in our samples, where the lack of long range diffusion during sintering reduces the possibility of pores spherodization) might extend the range of the region where the capillary condensation is possible, although it cannot extend beyond the limit for the formation of a continuous monolayer of physisorbed water molecules discussed before.

It must further be noted that at the lowest temperatures, where multilayer physisorption and capillary condensation are dominant, the protonic conductivity is observed in any sample, regardless of its grain size (see Figure 1) and even in pellets of not-sintered coarse powders.[46,52] In contrast, the specificity of bulk nanometric samples is in their ability to present a significant protonic conductivity even at intermediate temperatures, up to 300 °C.

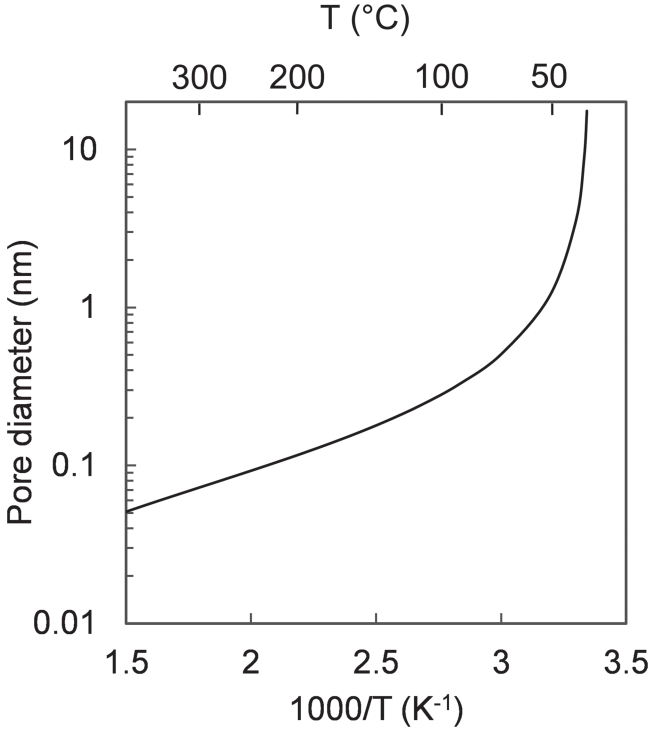

Figure 9. Limiting pore diameter required for condensation of water at different temperatures, considering a $P^{ex}_{H_2O} = 32$ mbar, calculated on the basis of the Kelvin equation.

As we mentioned before, at intermediate temperatures the oxides surface is mostly covered by a monolayer of strongly bonded hydroxyl groups. This is confirmed by our NMR measurements, showing indeed a fraction of tightly bonded hydroxyl groups that are retained even after annealing at temperatures up to 450 °C (see Figure 8). The role of the chemisorbed layer on the superficial ionic conductivity of oxides has been object of several investigations in the past, but it has never been completely clarified. A classical interpretation has been summarized by Anderson and Parks:[47] in this model mobile protons are produced through dissociation of the chemically bonded hydroxides; these H^+ can move by hopping between adjacent hydroxyl groups.[45,53] The ionization of the hydroxyl groups, however, is strongly dependent on the value of $P^{ex}_{H_2O}/P^{o}_{H_2O}$. The eventual presence of physisorbed water molecules allows the formation of H_3O^+, a specie that is far more stable than the bare proton. Furthermore, higher water coverage increases drastically the dielectric constant, lowering the dissociation energy. As a result, the presence of some physisorbed water, even in amounts not sufficient to produce a continuous film, can drastically enhance the conductivity deriving from hopping of protons originating from the dissociation of the chemisorbed hydroxide monolayer. This might explain the still large dependence on $P^{ex}_{H_2O}/P^{o}_{H_2O}$ of the conductivity for temperatures up to 150 °C, well above the temperature range where protonic conduction is ascribable to the presence of a multilayer physisorbed film. In the temperature range between 150 °C and 250 °C the conductivity appears to be almost independent from temperature: in this range the presence of physisorbed water molecules is minimal and the small loss of chemisorbed molecules[48,50] is probably compensated by the intrinsic increase of conductivity associated to the bare hydrogen hopping. Finally, for temperatures above 250 °C, an inversion in the temperature dependence is observed due to the predominance of the bulk ionic conductivity over the superficial component.

3.2. Role of Grain Size and Porosity

There are three more aspects associated with the data of Figure 1 that need some further consideration. These are: 1) the strong dependence of the conductivity on the grain size of the sample, 2) the unusually high value of the observed conductivities, and 3) the limited influence of the sample porosity. These three aspects must be discussed together as they are strongly interconnected.

Figure 1 shows as a reduction from 56 to 24 nm produces an increase of almost 4 orders of magnitude in the conductivity at 100 °C. Such a dramatic change cannot be explained on the basis of simple geometrical considerations. As shown by Avila-Paredes et al.[12] on the basis of a simple brick-layer model, the increase in grain boundary density scales only linearly with the inverse of the grain size. An alternative explanation can be proposed suggesting a modification in the surface characteristics of particles with a dimension in the lower nanometric range. It has recently been argued that in ionic materials a decrease in the grain size to the nanometric range can produce a modification in the space charge region in proximity of the surface.[43,54,55] It might be suggested that this

modification can produce a change in the ionization equilibria of the chemically adsorbed hydroxyl groups, or even of the physisorbed water molecules located above them. No direct proof of this hypothesis can be presented at this stage and further investigations are required. Although it has been evidenced that the structure of a very thin film of adsorbed water is very different from that of bulk liquid water,[56,57] the influence of such modifications on the protonic concentration and mobility is hard to predict, particularly in the case of nanoparticles of ionic materials. A possible evidence of such effect, however, can probably be found in the actual values of the specific conductivity presented by our samples. The specific conductivity of pure water exposed to air containing 300 ppm of CO_2 is $8.2 \cdot 10^{-7}$ Ω^{-1} cm^{-1},[58] while for our samples, when temperature is close to r.t., the data in Figure 1 show a specific conductivity in the range of 10^{-2} Ω^{-1} cm^{-1}. This value is surprisingly high, considering that the conduction is confined within a very small fraction of the sample, and it might be considered an indication of the increase in the dissociation equilibria of the adsorbed layer.

Regarding the influence of porosity on the sample conductivity, Figure 1 shows that an increase from 8 vol% to 25 vol% in porosity produces only a minimal variation on conductivity, for samples sintered at the same temperature (500 °C) and characterized by the same grain size (24 nm). This result seems quite surprising as such a large change in sample porosity is associated with a considerable variation in surface area, which is expected to produce a great influence in a conduction model based on surface phenomena. However, it must be considered that at constant pore size the surface area scales linearly with porosity. With this in mind, an increase of three times in the porosity is expected to produce a small variation on a logarithmic scale, where only variations of orders of magnitudes can be easily appreciated. The conductivity of the low-density samples (relative density 75 vol%) is approximately twice the conductivity of the high-density samples (relative density 92 vol%).

4. Conclusion

In conclusion, our experimental evidences allow us to present a possible interpretation for the low-temperature protonic conduction in bulk, high density, TiO_2 nanostructured anatase. This model is based on surface conduction through a percolative path, along the open residual nanoporosity left behind by the HP-FAST densification method. The observed conductivity can be explained on the basis of two distinct mechanisms depending on the temperature range. At the lowest temperatures the conductivity is associated to the movement of protons within a multilayer of water molecules physically adsorbed on the internal surfaces of the nanopores. This regime, however, can be sustained only until a continuous layer of physisorbed water molecules is present, probably up to a $P^{ex}_{H_2O}/P^{o}_{H_2O}$ ratio of 0.2, corresponding to a temperature of 55 °C in Figure 1. In this temperature range some level of the protonic conductivity is observed in any sample, regardless of its grain size, although the samples characterized by a smaller grain size show a higher conductivity.

At higher temperatures (T > 55 °C), where no continuous physisorbed water layer is present, the conduction probably derives from the jump of bare protons between adjacent clusters of physisorbed molecule or, at highest temperatures, between adjacent hydroxyl groups covering the surface as a result of water chemisorption. In the temperature range considered in this investigation (<450 °C), these hydroxyl groups are always present on the surface, although the coverage decreases gradually with temperature. The mobility of these protons is poorly characterized, but is probably significant as long as the surface coverage is fairly high. We can suggest that the dissociation equilibria of the chemically adsorbed hydroxyl groups are strongly dependent on the grain size in the lower nanometric range, as the characteristics of the space charge region adjacent to the surface change significantly with the grain size. This could also explain the enhanced conductivity of the samples with the smallest grain size, resulting in a level of conductivity unusually high when compared with pure water, indicating a significant increase in the concentration of the charge carriers.

It must finally be noted that the values of conductivity observed at the lowest temperatures for the nanometric TiO_2 are not much lower that the typical values shown by the perfluorosulfonic acid polymer membranes used in PEMFCs.[59] The use of low-temperature proton conductors based on simple inorganic oxides appears to be particularly promising as it would open the possibility to eliminate some typical drawbacks related to the use of polymeric membranes, such as safety issues or limited thermal stability.

5. Experimental Section

The sintering of the anatase nanopowder (Tronox Kerr McGee Chemicals AK1, >99.5% pure, 100% anatase, particle size 20 nm, specific surface area >90 m^2 g^{-1}) was performed using a homemade HP-FAST apparatus. In a typical experiment, TiO_2 powder (0.08 g) was loaded in a double stage die,[26,27] with an inner diameter of 5 mm. The high-pressure section of the die was made out of silicon carbide. Two kinds of samples have been produced: high-density samples were obtained using a pressure of 800 MPa, while low-density samples were obtained at 650 MPa, both for sintering time of 5 min. The resulting samples were typically 5 mm in diameter and with a thickness varying between 1.15 and 1.48 mm.

After sintering, the samples were annealed for 12 hours in a flowing dry oxygen atmosphere at 450°C in order to restore their oxygen stoichiometry.

Relative density was measured using geometric methods: for a sintering temperature of 500 °C, relative density of the porous and dense samples were 92 vol% and 75 vol% respectively; grain size was around 24 nm. For a sintering temperature of 550 °C, relative density of the porous and dense samples were 94 vol% and 75 vol% respectively; grain size was around 28 nm. High-density samples with grain sizes of 41 and 56 nm were obtained using a pressure of 800 MPa, raising the sintering temperatures to 600 and 690 °C, respectively.

Microstructural characterization of the samples was performed using a high-resolution scanning electron microscope (HR-SEM, TESCAN Mira 3) operated at 25 kV and by X-ray diffraction (XRD, Bruker D8 Advance). Grain size was evaluated from XRD data, using the Scherrer equation, and confirmed by SEM analysis, measuring at least 100 grains for each image, using the ImageJ software (version 1.43 m, W. Rasband, National Institutes of Health).

The porosity of the sintered samples was characterized by nitrogen adsorption. Specific surface area was determined using the BET

analysis, while the total pore volume and the pore size distribution were determined following the approach described by Lowell et al.[29]

The electrical conductivity has been characterized by AC impedance spectroscopy using a frequency response analyzer (FRA, Material Mates), in the frequency range between 1 and 10^6 Hz. Water incorporation was achieved by exposing the samples to O_2 saturated with water at 25 °C ($P^{ex}_{H_2O}$ = 32 mbar); the kinetics of water incorporation was estimated measuring the change in total resistance as a function of time at temperatures between 35 and 140 °C, from impedance measurements performed in the frequency range between 10^2 and 10^5 Hz.

The status of the water molecules absorbed by the samples was probed by DSC (DSC 2910, TA Instruments, New Castle, DE) and Solid state ^{1}H and ^{2}H NMR measurements, recorded on a 400 MHz spectrometer (Bruker, Avance III).

Further details can be found in the Supporting Information.

Supporting Information

Supporting Information is available from the Wiley Online Library or from the author.

Acknowledgements

The authors are grateful to Dr. Corrado Tomasi (Department of Chemistry, University of Pavia) for DSC analyses and to Laboratorio Arvedi (University of Pavia) for providing the TESCAN Mira 3 scanning electron microscope.

Received: February 7, 2014
Revised: April 2, 2014
Published online: May 30, 2014

[1] F. Maglia, I. G. Tredici, U. Anselmi-Tamburini, *J. Eur. Ceram. Soc.* **2013**, *33*, 1045.
[2] U. Anselmi-Tamburini, F. Maglia, G. Chiodelli, P. Riello, S. Bucella, Z. A. Munir, *Appl. Phys. Lett.* **2006**, *89*, 163116.
[3] H. J. Avila-Paredes, C.-T. Chen, S. Wang, R. A. De Souza, M. Martin, Z. Munir, S. Kim, *J. Mater. Chem.* **2010**, *20*, 10110.
[4] G. Chiodelli, F. Maglia, U. Anselmi-Tamburini, Z. A. Munir, *Solid State Ionics* **2009**, *180*, 297.
[5] S. Kim, U. Anselmi-Tamburini, H. J. Park, M. Martin, Z. A. Munir, *Adv. Mater.* **2008**, *20*, 556.
[6] S. Kim, H. J. Avila-Paredes, S. Wang, C.-T. Chen, R. A. De Souza, M. Martin, Z. A. Munir, *Phys. Chem. Chem. Phys.* **2009**, *11*, 3035.
[7] F. Maglia, I. G. Tredici, G. Spinolo, A. Tamburini, *J. Mater. Res.* **2012**, *27*, 1975.
[8] J. S. Park, Y. B. Kim, J. H. Shim, S. Kang, T. M. Gür, F. B. Prinz, *Chem. Mater.* **2010**, *22*, 5366.
[9] E. Ruiz-Trejo, J. A. Kilner, *J. Appl. Electrochem.* **2009**, *39*, 523.
[10] H. Takamura, N. Takahashi, *Solid State Ionics* **2010**, *181*, 100.
[11] S. Miyoshi, Y. Akao, N. Kuwata, J. Kawamura, Y. Oyama, T. Yagi, S. Yamaguchi, *Solid State Ionics* **2012**, *207*, 21.
[12] H. J. Avila-Paredes, J. Zhao, S. Wang, M. Pietrowski, R. A. De Souza, A. Reinholdt, Z. A. Munir, M. Martin, S. Kim, *J. Mater. Chem.* **2010**, *20*, 990.
[13] R. A. De Souza, Z. A. Munir, S. Kim, M. Martin, *Solid State Ionics* **2011**, *196*, 1.
[14] M. J. Pietrowski, R. A. De Souza, S. Kim, Z. A. Munir, M. Martin, *Solid State Ionics* **2012**, *225*, 241.
[15] M. Shirpour, G. Gregori, R. Merkle, J. Maier, *Phys. Chem. Chem. Phys.* **2011**, *13*, 937.
[16] K. Park, D. R. Olander, *J. Am. Ceram. Soc.* **1991**, *74*, 72.
[17] N. Sakai, K. Yamaji, T. Horita, H. Yokokawa, Y. Hirata, S. Sameshima, Y. Nigara, J. Mizusaki, *Solid State Ionics* **1999**, *125*, 325.
[18] T. Norby, M. Widerøe, R. Glöckner, Y. Larring, *Dalton Trans.* **2004**, *19*, 3012.
[19] F. M. Vichi, M. I. Tejedor-Tejedor, M. A. Anderson, *Chem. Mater.* **2000**, *12*, 1762.
[20] M. I. Tejedor-Tejedor, F. Maron Vichi, M. A. Anderson, *J. Porous Mater.* **2005**, *12*, 201.
[21] M. T. Colomer, *Adv. Mater.* **2006**, *18*, 371.
[22] G. Garcia-Belmonte, V. Kytin, T. Dittrich, J. Bisquert, *J. Appl. Phys.* **2003**, *94*, 5261.
[23] H. Ekström, B. Wickman, M. Gustavsson, P. Hanarp, L. Eurenius, E. Olsson, G. Lindbergh, *Electrochim. Acta* **2007**, *52*, 4239.
[24] N. Agmon, *Chem. Phys. Lett.* **1995**, *244*, 456.
[25] W. K. Chan, W. J. H. Borghols, F. M. Mulder, *Chem. Commun.* **2008**, 6342.
[26] U. Anselmi-Tamburini, J. E. Garay, Z. A. Munir, *Scr. Mater.* **2006**, *54*, 823.
[27] F. Maglia, M. Dapiaggi, I. G. Tredici, U. Anselmi-Tamburini, *Nanosci. Nanotechnol. Lett.* **2012**, *4*, 205.
[28] P. Knauth, H. L. Tuller, *J. Appl. Phys.* **1999**, *85*, 897.
[29] S. Lowell, J. E. Shields, M. A. Thomas, M. Thommes, *Characterization of Porous Solids and Powders: Surface Area, Pore Size and Density*, Kluwer-Springer, Dordrecht, The Netherlands **2010**.
[30] G. H. Findenegg, S. Jähnert, D. Akcakayiran, A. Schreiber, *Chem. Phys. Chem.* **2008**, *9*, 2651.
[31] S. Jähnert, F. Vaca Chávez, G. E. Schaumann, A. Schreiber, M. Schönhoff, G. H. Findenegg, *Phys. Chem. Chem. Phys.* **2008**, *10*, 6039.
[32] R. Böhmer, G. Diezemann, G. Hinze, E. Rössler, *Prog. Nucl. Magn. Reson. Spectrosc.* **2001**, *39*, 191.
[33] M. Vogel, *Eur. Phys. J. Spec. Top.* **2010**, *189*, 47.
[34] M. Vogel, P. Medick, E. A. Rössler, *Annu. Reports NMR Spectrosc.* **2005**, *56*, 231.
[35] A. Abragam, *Principles of Nuclear Magnetism*, Clarendon Press, Oxford, UK **1961**.
[36] V. M. Gun'ko, V. V. Turov, V. M. Bogatyrev, V. I. Zarko, R. Leboda, E. V. Goncharuk, A. A. Novza, A. V. Turov, A. A. Chuiko, *Adv. Colloid Interface Sci.* **2005**, *118*, 125.
[37] T. Tsukahara, W. Mizutani, K. Mawatari, T. Kitamori, *J. Phys. Chem. B* **2009**, *113*, 10808.
[38] B. Grunberg, T. Emmler, E. Gedat, I. Shenderovich, G. H. Findenegg, H.-H. Limbach, G. Buntkowsky, *Chem. Eur. J.* **2004**, *10*, 5689.
[39] C. A. Fyfe, *Solid State NMR for Chemists*, CFC Press, Guelph, Canada **1983**.
[40] G. M. German, *Sintering Theory and Practice*, Wiley, New York, London **1996**.
[41] D. Jiang, D. M. Hulbert, J. D. Kuntz, U. Anselmi-Tamburini, A. K. Mukherjee, *Mat. Sci. Eng. A* **2007**, *463*, 89.
[42] R. Orru, R. Licheri, A. Locci, A. Cincotti, G. Cao, *Mater. Sci. Eng. R* **2009**, *63*, 127.
[43] G. Gregori, M. Shirpour, *J. Maier, Adv. Funct. Mater.* **2013**, *23*, 5861.
[44] E. Traversa, *Sens. Actuators B Chem.* **1995**, *23*, 135.
[45] Z. Chen C. Lu, *Sens. Lett.* **2005**, *3*, 274.
[46] S. Raz, K. Sasaki, J. Maier, I. Riess, *Solid State Ionics* **2001**, *143*, 181.
[47] J. H. Anderson, G. A. Parks, *J. Phys. Chem.* **1968**, *72*, 3662.
[48] T. Morimoto, M. Nagao, F. Tokuda, *Bull. Chem. Soc. Jpn.* **1968**, *41*, 1533.
[49] M. Harju, T. Mäntylä, K. Vähä-Heikkilä, V.-P. Lehto, *Appl. Surf. Sci.* **2005**, *249*, 115.

[50] T. Morimoto, M. Nagao, F. Tokuda, *J. Phys. Chem.* **1969**, *73*, 243.
[51] J. J. Fripiat, A. Jelli, G. Poncelet, J. André, *J. Phys. Chem.* **1965**, *69*, 2185.
[52] M. Caldararu, G. Postole, C. Hornoiu, V. Bratan, M. Dragan, N. I. Ionescu, *Appl. Surf. Sci.* **2001**, *181*, 255.
[53] V. K. Khanna, R. K. Nahar, *J. Phys. Appl. Phys.* **1986**, *19*, L141.
[54] J. Maier, *Phys. Chem. Chem. Phys.* **2009**, *11*, 3011.
[55] J. Maier, *Adv. Mater.* **2009**, *21*, 2571.
[56] M. A. Henderson, *Surf. Sci. Rep.* **2002**, *46*, 1.
[57] G. E. Ewing, *J. Phys. Chem. B* **2004**, *108*, 15953.
[58] T. Seiyama, N. Yamazoe, H. Arai, *Sens. Actuators* **1983**, *4*, 85.
[59] S. J. Peighambardoust, S. Rowshanzamir, M. Amjadi, *Int. J. Hydrog. Energy* **2010**, *35*, 9349.